PHYSICAL REVIEW D VOLUME 53, NUMBER 11 1 JUNE 1996

Upper limit of the muon-neutrino mass and charged-pion mass from momentum analysis of a surface muon beam

K. Assamagan,[4,*] Ch. Brönnimann,[1,2] M. Daum,[1] H. Forrer,[1,3,†] R. Frosch,[1] P. Gheno,[1] R. Horisberger,[1]
M. Janousch,[1,2,‡] P.-R. Kettle,[1] Th. Spirig,[1,2,§] and C. Wigger[1,2]
[1] *Paul-Scherrer-Institut, CH-5232 Villigen-PSI, Switzerland*
[2] *Physik-Institut der Universität Zürich, Winterthurerstrasse 190, CH-8057 Zürich, Switzerland*
[3] *Institut für Teilchenphysik, Eidgenössische Technische Hochschule, CH-5232 Villigen-PSI, Switzerland*
[4] *Institute of Nuclear and Particle Physics, University of Virginia, Charlottesville, Virginia 22901*
(Received 15 December 1995)

We have determined the momentum p_{μ^+} of muons from the decay $\pi^+ \to \mu^+ \nu_\mu$ at rest, by analyzing a surface muon beam in a magnetic spectrometer equipped with a silicon microstrip detector. The result $p_{\mu^+} = (29.792\,00 \pm 0.000\,11)$ MeV/c leads to a squared muon-neutrino mass of $m^2_{\nu_\mu} = (-0.016 \pm 0.023)$ MeV^2, which corresponds to a ''laboratory'' upper limit of 0.17 MeV (C.L.=0.9) for the muon-neutrino mass. The cosmological upper limit of the neutrino mass (65 eV), the muon mass, and the new value of p_{μ^+} yield the pion mass $m_{\pi^+} = (139.570\,22 \pm 0.000\,14)$ MeV. Alternatively, if one does not use the cosmological upper limit of m_{ν_μ}, then a combined fit including the new p_{μ^+} value, and the m_{μ^+} and m_{π^-} values from other experiments and the CPT theorem ($m_{\pi^+} = m_{\pi^-}$) leads to $m_{\pi^\pm} = (139.570\,37 \pm 0.000\,21)$ MeV. As a side result, the mean kinetic energy of the pions stopped in the production target, made of isotropic graphite, immediately before their decay is found to be $\overline{T_{\pi^+}} = (0.425 \pm 0.016)$ eV. This is consistent with the hypothesis that the pions are trapped in the potential well of a spherical harmonic oscillator, $V(r) = V_0 + \frac{1}{2} k_s r^2$, with $k_s = (1.144 \pm 0.088) \times 10^{17}$ eV/cm^2.

PACS number(s): 14.60.Pq, 14.40.Aq, 14.60.Ef

I. INTRODUCTION

The question whether neutrinos have nonzero rest masses represents one of the most important problems of particle physics, and also of cosmology. In the present experiment, the main quantity to be determined is the mass m_{ν_μ} of the muon neutrino. This mass is derived from three quantities: namely, the momentum p_{μ^+} of the muon originating from the decay

$$\pi^+ \to \mu^+ \nu_\mu \tag{1}$$

at rest ($p_{\mu^+} \approx 29.79$ MeV/c ; measured in this experiment), and the masses of the negative pion m_{π^-} and the muon m_{μ^+} (measured in other experiments). The CPT theorem, implying that $m_{\pi^+} = m_{\pi^-}$, and four-momentum conservation in the decay (1) lead to the following equation for the squared muon-neutrino mass:

$$m_{\nu_\mu}{}^2 = m_{\pi^-}{}^2 + m_{\mu^+}{}^2 - 2 m_{\pi^-} (m_{\mu^+}{}^2 + p_{\mu^+}{}^2)^{1/2}. \tag{2}$$

The experimental uncertainty of the resulting squared neutrino mass is

$$\Delta(m_{\nu_\mu}{}^2) = [(\eta_1 \Delta m_{\pi^-})^2 + (\eta_2 \Delta m_{\mu^+})^2 + (\eta_3 \Delta p_{\mu^+})^2]^{1/2}, \tag{3}$$

where η_1 , η_2 , η_3 in Eq. (3) are partial derivatives of Eq. (2):

$$\begin{aligned} \eta_1 &\equiv \partial(m_{\nu_\mu}{}^2)/\partial m_{\pi^-} = 2(m_{\pi^-} - E_{\mu^+}) = 59.6 \text{ MeV}, \\ \eta_2 &\equiv \partial(m_{\nu_\mu}{}^2)/\partial m_{\mu^+} = 2 m_{\mu^+} [1 - (m_{\pi^-}/E_{\mu^+})] \\ &= -57.3 \text{ MeV}, \\ \eta_3 &\equiv \partial(m_{\nu_\mu}{}^2)/\partial p_{\mu^+} = -2 m_{\pi^-} p_{\mu^+}/E_{\mu^+} \\ &= -75.8 \text{ MeV}. \end{aligned} \tag{4}$$

Here, $E_{\mu^+} = (m_{\mu^+}{}^2 + p_{\mu^+}{}^2)^{1/2} = 109.78$ MeV is the total muon energy.

In the earlier measurements of p_{μ^+} at the Paul Scherrer Institute [1, 2], the muon momentum was determined to ± 18 ppm by use of a π^+ beam. In those experiments, stopped pion decays were made to occur in a small scintillator, placed in the homogeneous magnetic field of the muon spectrometer. In the present experiment, which was briefly described in Ref. [3], we used the same spectrometer magnet for the momentum analysis of a surface muon beam, i.e., a beam of muons from the decay (1) of π^+ mesons which are produced (by protons) in a pion production target and which come to rest near or at the surface of the same target, so that the decay muons can exit from it. The main advantage of using a surface muon beam is that the pion stopping density (number of stopped π^+ per g and sec) is 4 orders of magni-

---

[*] Present address: Department of Physics, Hampton University, Hampton, Virginia 23668.

[†] Present address: Seminar für Angewandte Mathematik, Eidgenössische Technische Hochschule, Rämistrasse 101, CH-8092 Zürich, Switzerland.

[‡] Present address: Institut für Teilchenphysik, Eidgenössische Technische Hochschule, CH-5232 Villigen-PSI, Switzerland.

[§] Present address: Paul-Scherrer-Institut Zürich, Badenerstrasse 569, CH-8048 Zürich, Switzerland.

0556-2821/96/53(11)/6065(13)/$10.00

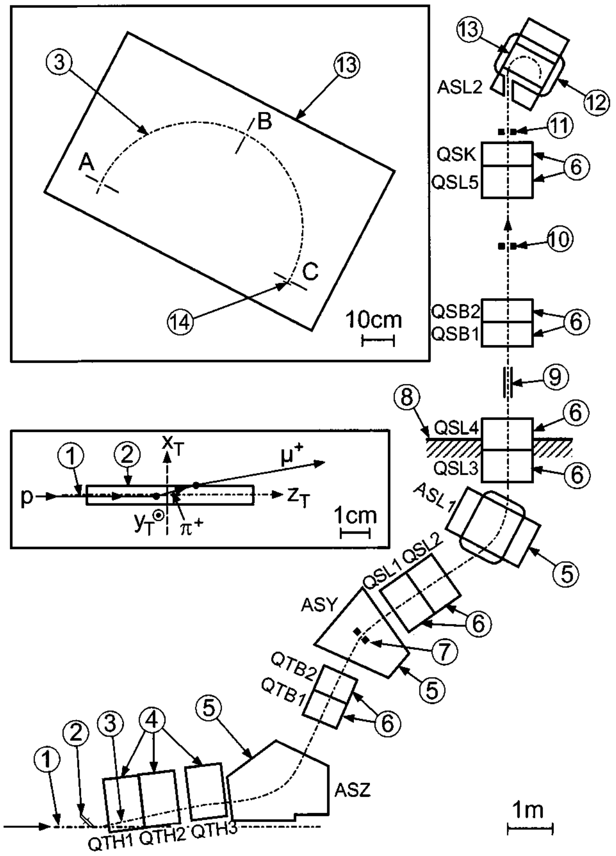

FIG. 1. Experimental setup. (1) Central trajectory of 590 MeV proton beam; (2) graphite target; (3) central trajectory of muon beam; (4) half-quadrupole magnets; (5) dipole magnets; (6) quadrupole magnets; (7) collimator defining the beam momentum acceptance; (8) concrete shielding of proton channel; (9) crossed-field particle separator; (10) lead collimator; (11) remotely movable collimator system (normally open); (12) magnetic spectrometer; (13) pole of spectrometer; (14) muon detectors (silicon microstrip and single surface-barrier detectors); A,B,C: copper collimators.

tude higher than in the older method [1,2]. Thus the momentum resolution of the muon spectrometer can be improved significantly by reducing the openings of the collimators, without causing the event rate to be too low. This resulted in a reduction of the p_{μ^+} uncertainty to ± 4 ppm.

In the following, the particle ν_μ is assumed to be in a mass eigenstate. If this should turn out to be wrong, the results would be approximately valid for that neutrino mass eigenstate which occurs most frequently in decay (1).

II. APPARATUS AND EXPERIMENTAL METHOD

A. General description

The measurements of p_{μ^+} were performed at the accelerator laboratory of the Paul Scherrer Institute. We used the secondary beam line $\pi E1$, shown schematically in Fig. 1. Protons with a kinetic energy of 590 MeV produce π^+ mesons in the production target E, a rotating-wheel device made of isotropic graphite. A small fraction of the produced pions are stopped in that same graphite target and decay nearly at rest. The range in graphite [density 1.75 g/(cm)^3] of the muons from the decay (1) at rest (momentum 29.79 MeV/c; kinetic energy 4.12 MeV) is 0.9 mm. Thus, if the decay occurs close to the surface of the target, and if the flight direction of the decay muons is such that the muon path length in graphite is less than 0.9 mm, the muons exit from the target. The momentum spectrum of the muons leaving the target extends from zero to the ‘‘free’’ p_{μ^+} value of 29.79 MeV/c. A part of these ‘‘surface muons’’ are transported in vacuum by the beam line $\pi E1$, composed of dipole and quadrupole magnets and a velocity separator, to the magnetic muon spectrometer. The magnets and the momentum-defining collimator of the channel were set to select positively charged particles in a 1% wide momentum band, ranging from 29.6 to 29.9 MeV/c. The separator, containing a horizontal electric field and a vertical magnetic field, was set such that the muons passed the lead collimator (item 10 of Fig. 1), whereas most of the positron contamination missed the collimator opening. The muon beam passes through a hole in the yoke of the muon spectrometer magnet and is focused onto the very narrow entry collimator A (width of opening 0.12 mm). Muons which pass the collimators A, B, and C are identified by a telescope composed of a silicon microstrip detector and a single silicon surface-barrier detector.

The magnetic field of the spectrometer is homogeneous, so that ‘‘horizontal’’ focusing occurs. The muon momentum spectrum mentioned above leads to a spatial distribution in the microstrip detector with a sharp cutoff near the center of the detector, corresponding to the maximal muon momentum p_{μ^+}. This momentum is derived from the position and shape of the cutoff in the event distribution of the microstrip detector.

B. The production target

The stopped pion decays to be studied occurred in the graphite target (item 2 of Fig. 1). The target is a wheel which rotates with one revolution per sec, so that the temperature of the graphite (type EK90 from Ringsdorff-Werke, Bonn, Germany; density = 1.75 g/cm^3) is not increased too much by the proton beam. During the data taking runs, the graphite temperature was 990–1270 K, depending on the proton beam current (200–550 μA). The target has the shape of a truncated cone. The lower of the two insets in Fig. 1 represents a horizontal cut at beam height through the target, which is 60 mm long in the proton beam direction, and 6 mm wide. The target was grounded; the electrical resistance between the graphite surface and the steel support of the target assembly was measured to be 1 Ω.

The horizontal and vertical proton beam profiles at the production target both had a standard deviation of 0.9 mm. The spatial distribution of π^+ stops in the graphite target was calculated by a Monte Carlo program, as described in Refs. [4, 5]; see also Sec. IV A below.

C. The muon beam line

Typical muon beam envelopes, which were calculated by the computer program TRANSPORT [6], are shown in Fig. 2. For this calculation, a narrow source of muons was assumed in order to clearly exhibit the focusing conditions. The coordinate s is measured along the central trajectory of the channel. The production target is at $s=0$. At $s\approx 14$ m the beam

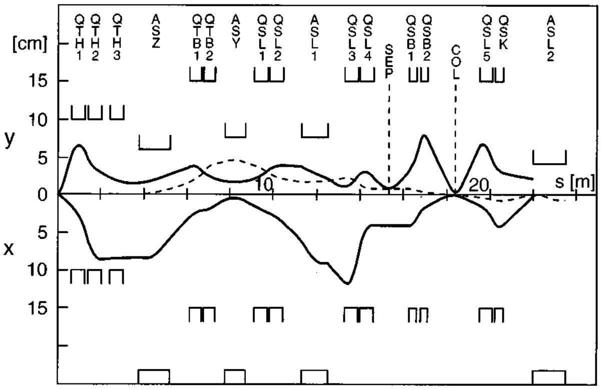

FIG. 2. Muon beam calculated by the computer program TRANSPORT [6]. The solid curves represent the horizontal (x) and vertical (y) envelopes. The dashed curve is the dispersion trajectory ($p = 1.01 p_0$).

leaves the concrete shielding and enters the $\pi E1$ area; cf. Fig. 1. The entry collimator of the muon spectrometer is at $s = 22.2$ m, and the muon detectors are at s=23.3 m. The dashed trajectory in Fig. 2 is the dispersion trajectory, i.e., a trajectory which starts at the same place and with the same direction as the central trajectory, but has a momentum of 1.01 p_0 (where p_0 is the momentum of the central trajectory). Between $s = 4$ m and $s = 18$ m, the dispersion trajectory has a negative x coordinate.

The main features of the tune shown in Fig. 2 are (a) a double waist at the momentum-defining collimator, located at the center of the dipole magnet ASY ($s = 8.2$ m); (b) at the separator ($s = 15.4$ m) there is a narrow waist in the magnetic-field direction of the separator (y), while in the electric-field direction (x) the beam has a small divergence; (c) the quadrupole doublet (QSB1,QSB2) is polarized so that the unwanted particles (e^+) move away from the central trajectory after QSB2, and thus are suppressed efficiently by the lead collimator at $s = 18.4$ m; (d) a narrow horizontal waist at the entry collimator of the muon spectrometer ($s = 22.2$ m); and (e) at this entry collimator, the dispersion trajectory coincides with the central trajectory both in position and in direction.

D. The muon spectrometer

The spectrometer is shown in Fig. 1 and also, in greater detail, in Fig. 3. The magnet was originally a standard beamline element of ASL-type, with a pole area of 60 × 100 cm^2 and a pole gap of 9 cm. The shimming of this magnet and the computer-controlled turn-on procedure are the same as in the previous p_{μ^+} measurements [2,8]. During data taking, the magnetic field was set to values around 0.276 T. In the following, we describe the changes made for the surface-muon beam experiment.

As shown in Fig. 3, the muon beam entered the spectrometer through a hole cut through the iron yoke of the magnet. The angle between the axis of the hole and the normal to the outer surface of the yoke (27 °) was chosen such that muons entering the hole on the axis have the appropriate flight direction at the entry collimator A (item 4 of Fig. 3). The collimators A, B, C are made of copper and have rectangular openings. The widths of the collimator openings were 0.12 mm (collimator A), 10.0 mm (B), and 14.0 mm (C). All three collimator openings had a height of 10.0 mm. The collimator thickness at the edge of the opening was 0.3 mm for A and B, and 1.0 mm for C.

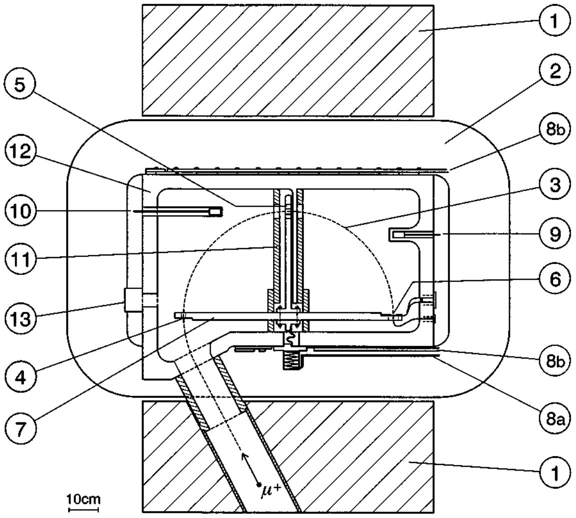

FIG. 3. The muon spectrometer: (1) magnet yoke; (2) magnet coils; (3) central muon trajectory; (4)–(6) copper collimators A,B,C; (7) titanium support; (8a) and (8b) cooling water pipes; (9) and (10) NMR probes; (11) lead shielding; (12) vacuum chamber; (13) port for vacuum pump.

The region of collimator C is shown on a larger scale in Fig. 4(a). The 4.1 MeV muons lose about 0.9 MeV in passing through the 0.28 mm thick silicon microstrip detector [7] (cf. Sec. II E below) and are then stopped in the 1 mm thick depletion layer of the single silicon surface-barrier detector. The corresponding large signals from this latter detector (3.2 MeV) were used as an event trigger for the data taking electronics.

The collimators A, B, C and the silicon detectors were mounted on a support (item 7 of Fig. 3) made of titanium, selected from among the materials fulfilling the magnetic and mechanical requirements because of its small thermal expansion coefficient. The most important distances to be measured were those between the edges of collimator A and the individual microstrips (about 72 cm). They were determined to ±1 ppm in a temperature-controlled measuring room equipped with a precision carriage, a microscope and a laser interferometer. The temperature of the titanium support was kept between 293.1 K and 293.5 K both during the beam runs and the distance measurements, and was continuously recorded by four probes distributed over the support.

Before and after the beam runs, the magnetic field in the region of the muon trajectories was mapped with nuclear-magnetic-resonance (NMR) probes. During these measurements and also during the data taking, the field was stabilized by feedback from a fixed NMR probe (item 9 of Fig. 3). The slight drifts of the field distribution were monitored continuously by a second fixed NMR probe (item 10 of Fig. 3).

E. The silicon microstrip detector

The silicon microstrip detector is schematically shown in Fig. 4(b). A 280 μm thick silicon crystal is used as base

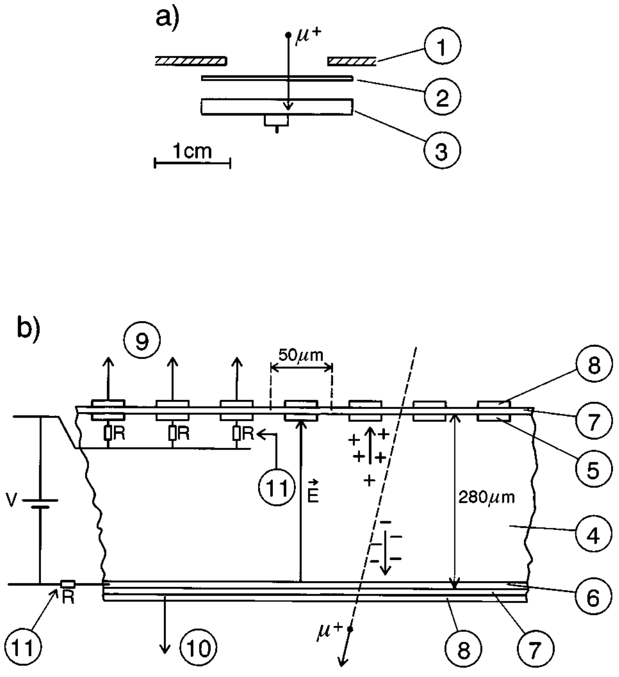

FIG. 4. (a) Details near collimator C (item 6 of Fig. 3): (1) copper collimator; (2) silicon microstrip detector; (3) single silicon surface-barrier detector. (b) Schematic of microstrip detector: (4) silicon crystal (n-type); (5) implanted boron (p^+ type); (6) implanted phosphorus (n^+ type); (7) silicon oxide (insulator); (8) aluminium electrodes; (9) conductors for upstream-side readout; (10) conductor for downstream-side readout; (11) poly-silicon bias resistor. The voltage V amounted to about 60 V.

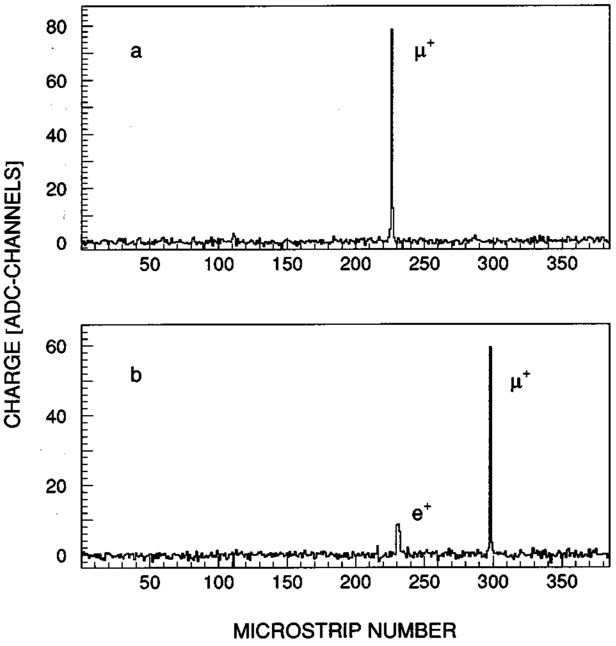

FIG. 5. Charge distribution over the 384 strips of the microstrip detector, for two typical events; cf. Sec. III A of text.

material. On the upstream face, 384 vertical strips of 25 μm width and 19.2 mm length are implanted (p^+-doped silicon with boron). The pitch of those strips, and therefore the effective strip width, is 50 μm. The implanted strips are capacitively coupled to 25 μm wide aluminium strips, which yielded the muon momentum spectra to be presented in Sec. III below. The downstream face is divided into 384 horizontal strips (n^+-type silicon with phosphorus), which were used to determine the vertical muon distribution. The voltage applied between the downstream and upstream strips was around 60 V. At this voltage, the n-doped silicon substrate is fully depleted. The microstrip detector and its electronics are described in detail in Ref. [7].

III. EXPERIMENTAL MUON SPECTRA

A. Microstrip detector signals

The trigger signals generated by beam muons in the surface barrier detector (item 3 of Fig. 4) started the readout of the 384 channels of the microstrip detector. The resulting charge distributions for two events are shown in Fig. 5. In the event of Fig. 5(a), the muon generated a single narrow peak. In a few percent of the events, the positron from the stopped muon decay in the nearby surface-barrier detector was also registered by the microstrip detector; see Fig. 5(b). For further analysis, the number of the strip with the highest charge was used [e.g., strip 226 for Fig. 5(a), strip 298 for Fig. 5(b)]. We rejected a few percent of the events, in which the peak charge was below one-half of its normal value [9]. In these events, the trigger pulse in the surface barrier counter was generated not by a muon, but by a positron from the decay of a stopped μ^+ or by a β particle from the decay of a radioactive residual gas atom.

B. Momentum spectra of μ^+

Three typical spectra, each obtained in about 1 h of data taking time, are shown in Fig. 6. One microstrip width (0.05 mm) corresponds to a relative momentum bite of $\Delta p/p = 6.9\times10^{-5}$.

In the case of Fig. 6(a), the beam magnets and the spectrometer were set to a central momentum of 29.45 MeV/c, around which the momentum distribution of muons leaving the production target is approximately uniform. For Figs. 6(b) and 6(c), the central momentum was set to 29.75 MeV/c, so that the sharp cutoff at 29.79 MeV/c is visible.

The opening of collimator C (item 1 of Fig. 4) corresponds to strips 40–320. The approximately linear rise in strips 117–150 of Fig. 6(a) is due to the upper end of the beam momentum bite, defined by the momentum slit of the channel (item 7 of Fig. 1). The extension of that rise corresponds to the monochromatic beam-spot size at the momentum slit. The distribution in strips 150–260 of Fig. 6(a) is approximately uniform. Slight changes of the beam magnet settings lead to considerable deviations from uniformity, mostly because the dispersion trajectory at the entry of the spectrometer differed from the ideal case shown in Fig. 2. Such deformations were also caused by drifts of the beam-magnet fields. The roughly linear fall in strips 260–290 corresponds to the lower end of the beam momentum bite.

In Fig. 6(b), the beam momentum bite corresponds to strips 120–287. The right part of the spectrum (strips 180–320) is similar to Fig. 6(a). At strips 177–183 of Fig. 6(b), one sees the sharp cutoff related to the ''free'' muon momen-

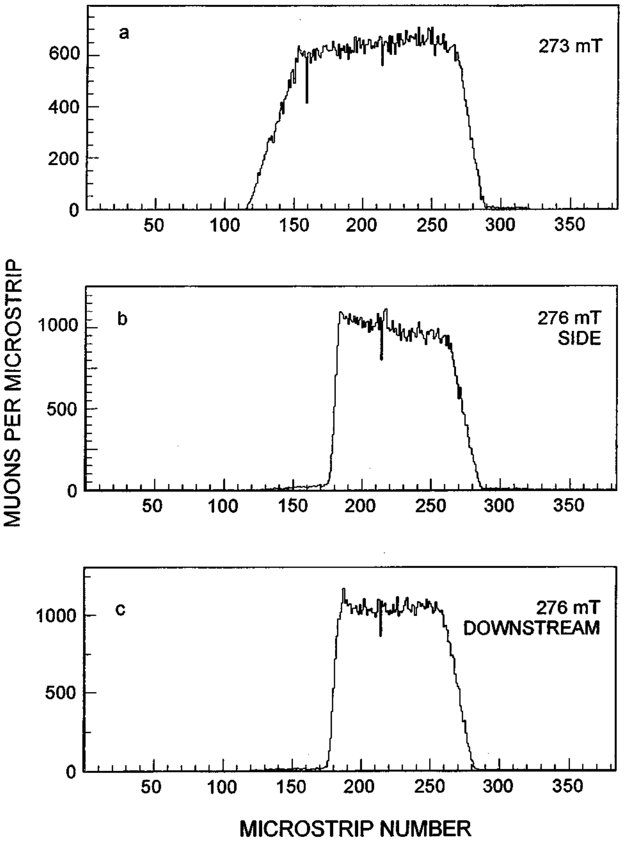

FIG. 6. Distribution of muons in the microstrip detector for three typical runs. (a) Central muon-beam momentum 29.45 MeV/*c*, spectrometer field 273.0 mT; (b) and (c) central muon-beam momentum 29.75 MeV/*c*, spectrometer field 276.0 mT. One microstrip width (0.05 mm) corresponds to $\Delta p_{\mu^+} \approx 0.0021 \mathrm{MeV}/c$. The muon momentum increases to the left. For details, see Sec. III B.

tum of 29.79 MeV/*c* (see Sec. II A above). The peak at strip 185 can be understood by consideration of the energy loss straggling of muons in the graphite target (cf. Sec. IV B). The weakly populated distribution in strips 120–175 of Fig. 6(b) is due to ''cloud muons,'' i.e., to muons from the decay of pions in flight near the production target. The events in strips 290–320 are due to muons scattered in the jaws of the copper collimators A and B. This background distribution is discussed in Sec. IV D below.

The spectrum of Fig. 6(b) contains muons from the side surface of the production target, whereas that of Fig. 6(c) contains muons from the downstream surface; see Sec. IV A. Both of these spectra were obtained with a spectrometer field of 276.0 mT. In total, we recorded 44 muon spectra in the ''cutoff'' region [i.e., similar to Figs. 6(b) and 6(c); central beam momentum 29.75 MeV/*c*]. Twenty-two of these spectra contained muons from the downstream surface of the production target and were used to determine the momentum p_{μ^+}, while the 22 spectra of muons from the side surface were used to check the corrections related to the reduced pion stop density near the target surface (cf. Sec. IV A). In each of these two groups of 22 spectra, six different spectrometer fields were used, namely 275.4, 275.6, . . . , 276.4 mT.

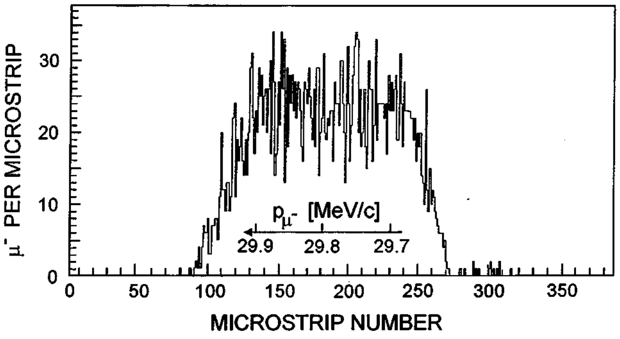

FIG. 7. Distribution of negative muons in the microstrip detector. Central μ^--beam momentum 29.80 MeV/*c*, spectrometer field 276.0 mT.

C. Momentum spectra of μ^-

As a test, we inverted the field of the beam magnets and the spectrometer, so that negative muons were accepted. The resulting μ^- spectrum, obtained at $p(\text{beam}) = 29.8$ MeV/*c* and $B(\text{spectrometer}) = 276.0$ mT [i.e., same absolute magnitude of field as in Figs. 6(b) and 6(c)] is shown in Fig. 7. In this case the event rate was 2 orders of magnitude lower than in the case of Fig. 6. Since π^- mesons stopped in the graphite target form pionic carbon atoms and are quickly captured by carbon nuclei, decays of stopped π^- are very rare. The spectrum of Fig. 7 consists almost entirely of ''cloud'' muons, originating from π^- decays in flight, and thus has no significant step at 29.79 MeV/*c*. The approximately uniform shape of that spectrum agrees with theoretical predictions, thus confirming the reliability of the similar calculation of the cloud μ^+ background below the cutoff momentum [e.g., in strips 180–230 of Figs. 6(b) and 6(c)], where the μ^+ spectra are dominated by π^+ decay at rest.

IV. MONTE CARLO CALCULATIONS

A. Pion stopping density

As mentioned in Sec. II B above, the spatial distribution of π^+ stops in the graphite production target was calculated by a Monte Carlo program [4,5]. We used pion-production cross sections measured by Crawford *et al.* [10,11], and applied the formulae of Ziegler *et al.* [12] for the stopping of ions to π^+ mesons.

The path of a pion produced in the graphite target and stopped in the same target is divided into three phases [4]. The first phase reaches from the production of the pion to its ''3 keV point,'' i.e., to the point where the kinetic energy of the pion is reduced below 3 keV. In that first phase, the path of the pion through the graphite is well approximated by a straight line. The resulting spatial distribution of the 3 keV points at the target surface is shown in Fig. 8.

In the second phase, the pion is slowed down from 3 keV to 10 eV. In that energy region, the pion can be scattered through large angles. As a consequence (since pions having exited from the target into the surrounding vacuum are not scattered back), the density of the 10 eV points is smaller in the outermost few nanometers than further inside the target, as shown in Fig. 9. The results are not changed significantly if the limiting energy of 10 eV is changed to 5 or 20 eV [4].

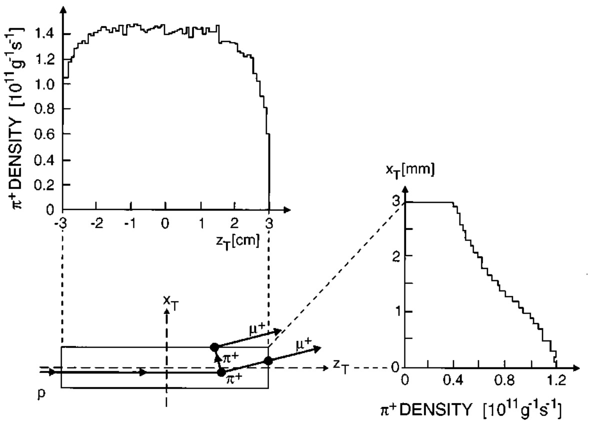

FIG. 8. Monte Carlo results for the density of the ''3 keV points'' of π^+ mesons at the surface of the graphite production target (item 2 of Fig. 1), for a 590 MeV proton beam current of 280 μA; cf. Sec. IV A.

In the third phase, the pion moves with a kinetic energy of about 10 eV to a trapping site. Most of the carbon atoms of the target belong to ''crystallites,'' i.e., to single graphite crystals of about $(35\ \mathrm{nm})^3$. If the 10 eV point of the pion lies inside of such a crystallite, the pion will move by diffusion, between two planes of the graphite crystal, to a trapping site at the surface of the crystallite [13]. Pions with a 10 eV point in the amorphous carbon between the crystallites are trapped at similar sites. The hypothesis that the pions end up at such trapping sites is supported by measurements of the solubility of low-pressure hydrogen gas in hot graphite [14]: The hydrogen solubility is much larger in graphites with small crystallites than in those with large crystallites, indicating that the protons of the hydrogen gas, and also the positive pions of our experiment, are preferentially trapped at the surface rather than the inside of the crystallites. Additional confirmation of this trapping hypothesis came from the shape of our muon momentum spectra; cf. Sec. V E below.

For the trapping site distribution of π^+, the calculated ''surface shifts'' (defined similarly to the shift Δx shown in Fig. 9) were [5]

$$\Delta z = (5.6 \pm 2.5)\ \ \mathrm{nm} \tag{5}$$

at the downstream surface, and

$$\Delta x = (5.9 \pm 2.5)\ \ \mathrm{nm} \tag{6}$$

at the side surface. The uncertainties in Eqs. (5) and (6) are mainly due to the possibility that the trapping of a pion at a crystallite boundary at the target surface may be less probable (by an unknown amount) than the trapping at a crystallite boundary inside the target [4].

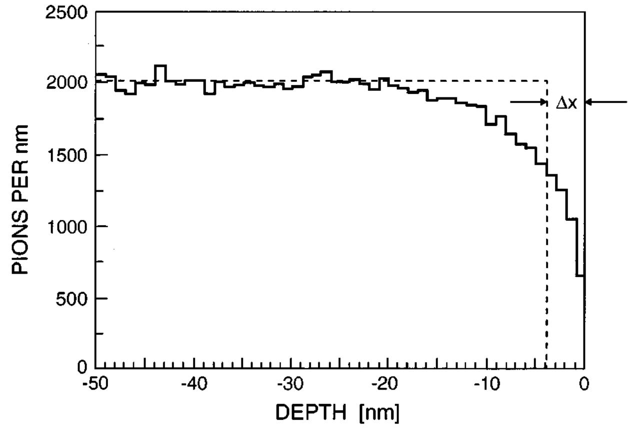

FIG. 9. Monte Carlo density of the ''10 eV points'' of π^+ mesons in the outermost 50 nm of the graphite target. The area of the dashed rectangle is equal to that of the histogram.

Since the ''effectively pionless'' surface layers defined by Eqs. (5) and (6) are crossed by the muons at very different angles (10° and 80°; cf. Fig. 8), one expects that the p_{μ^+} result obtained from the experimental spectra of muons from the downstream surface under the assumption of an exactly uniform π^+-trapping distribution is larger than that for muons from the side surface. If the surfaces of the target are assumed to be perfectly smooth, the predicted results are smaller than the true p_{μ^+} value by

$$\delta p(\text{smooth, downstream}) = (0.052 \pm 0.023)\ \ \mathrm{keV}/c \tag{7}$$

for muons from the downstream surface, and by

$$\delta p(\text{smooth, side}) = (0.31 \pm 0.13)\ \ \mathrm{keV}/c \tag{8}$$

for muons from the side surface [5]. The uncorrected result for the downstream surface is thus predicted to be larger than that for the side surface by

$$Dp(\text{smooth}) = (0.26 \pm 0.13)\ \ \mathrm{keV}/c$$

$$[(8.8 \pm 4.5)\ \ \mathrm{ppm}]. \tag{9}$$

Under the more realistic assumption of grainy surfaces (graphite grain diameter 50 μm) the Monte Carlo predictions are [5]:

$$\delta p(\text{grainy, downstream}) = (0.050 \pm 0.022)\ \ \mathrm{keV}/c, \tag{10}$$

$$\delta p(\text{grainy, side}) = (0.106 \pm 0.045)\ \ \mathrm{keV}/c, \tag{11}$$

$$Dp(\text{grainy}) = (0.056 \pm 0.050)\ \ \mathrm{keV}/c$$

$$[(1.9 \pm 1.7)\ \ \mathrm{ppm}]. \tag{12}$$

In order to confirm experimentally the calculated difference given by Eq. (12), we took advantage of the structure shown in Fig. 8: The pion density has a first maximum near the center of the side surface (x_T=0.3 cm; z_T=0), and a second maximum at the center of the downstream surface (x_T=0; z_T=3 cm), while at the corner (x_T=0.3 cm; z_T=3 cm) the density has a sharp minimum. As shown in Fig. 10, this structure (which was imaged by the beam transport magnets onto the very narrow entry collimator A of the muon spectrometer) was confirmed by measurements of the muon rate in the spectrometer as a function of the current settings of the dipole magnets in the secondary beam channel.

As mentioned in Sec. III B, half of our muon spectra contained muons from the side surface of the production target, while the other half contained muons from the downstream surface. The two surface regions were selected by use of the dipole magnets of the beam line, i.e., by choosing one of the

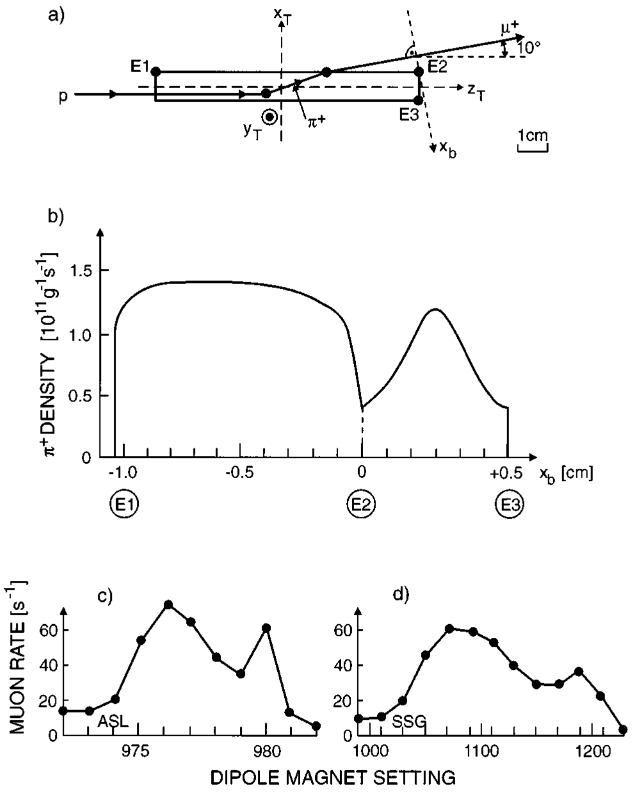

FIG. 10. (a) Sketch of the production target; E_1–E_3: corners of target; x_b: horizontal coordinate, perpendicular to muon beam. (b) The Monte Carlo π^+ density of Fig. 8, plotted vs the coordinate x_b. (c) Experimental muon rate vs setting of the dipole magnet ASL1 (cf. Fig. 1). (d) Muon rate vs setting of the dipole magnet SSG of the crossed-field separator (item 9 of Fig. 1). The shapes of the curves (c) and (d) are consistent with the source profile (b).

two peaks in Fig. 10(c) or 10(d). The results of the comparison of the two groups of spectra are presented in Sec. V D.

B. Muon energy loss

A second Monte Carlo program was used to generate the energy loss of the muons on the way from their creation by the decay of stopped π^+ in the graphite target to the point where they exit into the vacuum. For this calculation, the π^+ stopping density in the relevant surface regions of the production target was assumed to be uniform, i.e., the ‘‘surface shifts’’ of Eqs. (5) and (6) above were neglected. Our method of calculating the momentum spectrum of the exiting muons [9] is similar to that of Bichsel [15]. The free path of the 4.1 MeV muon to the next energy loss process in the graphite is generated from an exponential distribution with a mean free path of 25 nm. The total path of the relevant muons in the target ranged from zero to about 40 μm. Three different energy loss processes were considered, namely (a) the collision of the muon with a K electron of a carbon atom, (b) the collision with an individual L electron, and (c) the generation of a plasmon, i.e., a quantum of the collective oscillation of the electron gas formed by the L electrons.

The resulting muon-momentum spectrum is shown in Fig. 11. An inital momentum of 29.792 MeV/c was assumed. The peak at 792.0 keV/c in Fig. 11(b) contains those muons which leave the target without energy loss, and the peak at 791.9 keV/c contains muons which have produced one plasmon (plasmon energy ≈ 25 eV). In Fig. 11(a), the momentum bins are wider, so that the details visible in Fig. 11(b) are not resolved. The peak at 29.79 MeV/c in Fig. 11(a) is similar to that predicted for pions stopped in organic scintillators; see, e.g., Fig. 12 of Ref. [2].

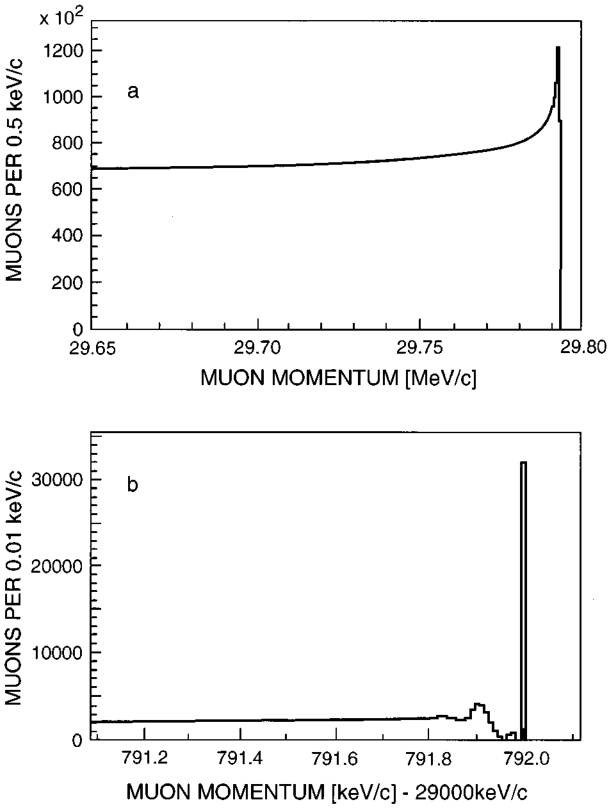

FIG. 11. End-point region of the Monte Carlo calculated momentum spectrum of muons leaving the production target; cf. Sec. IV B.

C. Muon spectra at the microstrip detector

The spatial muon distribution at the microstrip detector was predicted by use of a third Monte Carlo program. In this

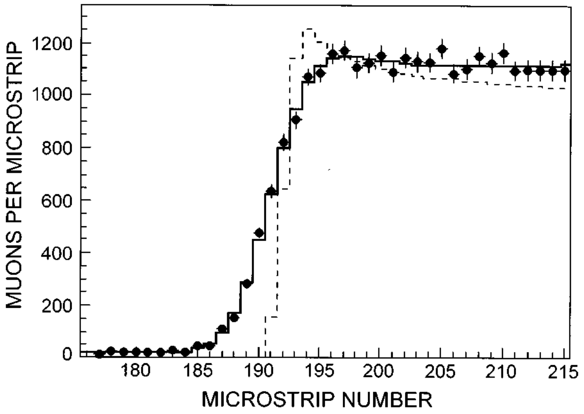

FIG. 12. Distribution of muons in the microstrip detector; spectrometer field 276.2 mT. Dots: experimental data; dashed (solid) histogram: raw (fitted) Monte Carlo distribution; cf. Secs. IV C and V B.

calculation, the muon-momentum spectrum shown in Fig. 11 was assumed to be valid also at the entry collimator A of the spectrometer (item 4 of Fig. 3). The distributions of the TRANSPORT variables [6] x, y, θ, and ϕ were assumed to be uniform at point A (x,y see Fig. 2; θ,ϕ, directional angles of the muon momentum vector). The uniformity of the θ and ϕ distributions was confirmed experimentally by recording the muon rate as a function of the positions of the four independently movable jaws of a collimator (item 11 of Fig. 1) located 1.5 m upstream of A. The uniformity of the x and y distributions was confirmed by recording the muon rate as a function of the settings of horizontal and vertical bending magnets. In the present simulation, a muon was considered as lost if it missed the opening of the collimator A, B, or C. Slit scattering is treated in Sec. IV D below. The magnetic field of the spectrometer was assumed to be uniform and equal to the weighted mean of the distribution, as mapped by NMR probes, over the region of the accepted muon trajectories. The method of calculating that mean field is described in Ref. [2]. Our simplifying assumption of uniformity was found, by a study of second-order beam optics in approximately homogeneous magnetic fields [16], to have a negligible influence on the p_{μ^+} result.

The obtained Monte Carlo event distribution for a reference field of 276.2 mT is shown by a dashed histogram in Fig. 12. This histogram differs strongly from the experimental distribution (shown by dots). The changes applied to the Monte Carlo distribution in order to obtain a good fit to the data (solid histogram in Fig. 12) are discussed in Sec. V B below.

D. Slit scattering

A fourth Monte Carlo program was used to calculate the microstrip distribution of muons which are scattered in the jaws of the copper collimators A and B of the spectrometer. These copper jaws were approximated by 2000 infinitesimally thin sheets of the appropriate position, shape, and surface density (in g/cm^2). If a muon hits such a sheet, the change of its momentum vector due to multiple Coulomb scattering and ionization energy loss (including energy loss straggling) is generated. The results do not change significantly if the number of thin sheets per collimator is lowered from 2000 to 1000. For this calculation, the muon-momentum spectrum upstream of collimator A was assumed to be uniform, extending from 29.613 to 29.792 MeV/c. The resulting distribution at the microstrip detector for scattered and nonscattered muons is shown in Fig. 13. The scattered muon distribution in strips 290–320 is consistent with the experimental spectra [Figs. 6(b) and 6(c)]. In the microstrips relevant for the determination of p_{μ^+} (numbers 190–220 in the case of Fig. 13), the number of scattered muons is seen to be only about 1×10^{-3} of the number of nonscattered muons.

E. Charge distribution in the microstrip detector

Our fifth Monte Carlo simulation concerned the distribution of the charge registered in the strips of the microstrip detector for a given muon hit location. We took into account the multiple scattering of the muons in the detector, the diffusion of the charge carriers, their deflection in the magnetic field of the spectrometer, and the noise superimposed onto the registered charge. This simulation is described in Ref. [9]. The results are summarized in Secs. V E and V F below.

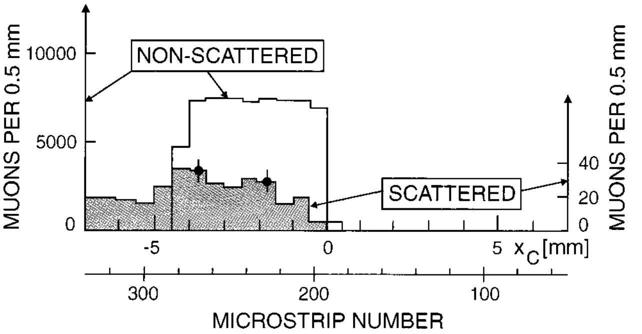

FIG. 13. Monte Carlo distribution of muons scattered in the collimators A,B (cf. Fig. 1).

V. ANALYSIS OF EXPERIMENTAL SPECTRA

A. Microstrip efficiencies

For the determination of p_{μ^+}, the microstrips 130–250 are of interest. As visible in Fig. 6, there are two bad strips in that range, namely numbers 159 and 214, the contents of which are systematically low. The nature of the fault was found to be different in the two cases. In strip 159, the discharge time constant (bias resistance times coupling capacitance) was measured to be abnormally small. Under the microscope, this was seen to be the result of a damaged aluminium electrode, leading to a small coupling capacitance. Signals from muons which hit this strip have a reduced charge and decay fast because of the small time constant, so that a fraction of the events fall below the discrimination level set in the analysis. Valid results were obtained by simply omitting strip 159 from the fits of the microstrip distributions (cf. Sec. V B below). In strip 214, an abnormally high resistance (inferred from a large measured time constant) was the result of a broken poly-silicon bias resistor. The drift field at this strip is deformed, which causes a proportion of the events to be attributed to the neighboring strips. In this case, we replaced the contents of strips 212–216 by their average. This was acceptable because strip 214 was in a nearly uniform part of the spectrum in all cases.

For the remainder of the relevant strips, the relative efficiencies were found to be close, but not exactly equal to unity. Polynomials were fitted to the sum of all spectra taken at reduced beam momenta [e.g. Fig. 6(a)]. The χ^2 values of those fits were larger than 1.0 per degree of freedom. This was not due to a systematic trend, but to an apparently random fluctuation of the numbers of events in excess of the uncertainty originating from counting statistics. As a consequence, for further analysis the uncertainty of the number of events n_i in strip i was defined to be [9]

$$\Delta n_i=[n_i+(0.014n_i)^2]^{1/2}. \tag{13}$$

B. Fits of the microstrip distributions

The histogram drawn as a solid line in Fig. 12 was derived from the ‘‘raw’’ Monte Carlo distribution (dashed line) by use of the minimum-finding computer program MINUIT [17]. Five free parameters were varied to obtain the best fit to the experimental numbers of muons per microstrip.

(1) A normalization factor by which all Monte Carlo numbers of events were multiplied.

(2) A horizontal shift applied to the Monte Carlo histogram. This corresponds to a change of the initial muon momentum p_{μ^+} from its assumed value of 29.792 MeV/c.

(3) A constant background attributed to cloud muons (cf. Sec. III B), which was added to each bin of the Monte Carlo histogram.

(4) The standard deviation of a Gaussian distribution with which the Monte Carlo histogram was folded. This is justified in Sec. V E below.

(5) The coefficient a of a linear correction factor $f(i)=1.0+a[i-i_0]$ (where i is the microstrip number, and i_0 is a fixed number, chosen to be at the peak of the distribution), by which the Monte Carlo numbers of events were multiplied. The factor $f(i)$ was introduced in order to correct possible deviations of the beam optics from the ideal case shown in Fig. 2. The choice of a second-order polynomial for the factor $f(i)$ did not change the results significantly, nor did it improve the fits.

The small background due to slit scattering (cf. Sec. IV D) was taken into account, with sufficient precision, by the free parameters (3) and (5). The results to be quoted below were obtained by including 40 strips into the fits, e.g., as shown in Fig. 12. Changes of the number of included strips to 30, 50, or 60 did not lead to significantly different results. The χ^2 value of the fit shown by the solid histogram in Fig. 12 is 35.0 for 35 degrees of freedom.

The model with the five free parameters defined above gave good fits to the experimental data: For the 22 spectra (similar to that in Fig. 12) of muons from the downstream surface of the production target, the χ^2 value for 35 degrees of freedom was 23.1 in the best case, and 43.8 in the worst case. The average of the 22 χ^2 values was 35.5 [9]. The corresponding χ^2 values for the 22 spectra of muons from the side surface were 21.1 (best), 45.9 (worst), and 32.7 (average).

C. Averages of the fitted parameters

The p_{μ^+} results obtained by MINUIT [17] from the 22 experimental momentum spectra of muons from the downstream surface of the production target have a weighted mean of

$$p_{\mu^+}(\text{downstream})=(29.791\,937\pm 0.000\,047)\ \text{MeV}/c. \quad (14)$$

The χ^2 value of the 22 p_{μ^+} values with respect to that mean is 29.1 for 21 degrees of freedom. The weighted mean of the 22 p_{μ^+} values for the side surface is

$$p_{\mu^+}(\text{side})=(29.791\,935\pm 0.000\,045)\ \text{MeV}/c, \quad (15)$$

with $\chi^2=29.6$ (21 DF).

In Fig. 14, the p_{μ^+} results obtained for each of the six different spectrometer settings are plotted. As shown by Figs. 6 and 12, the cutoff dominating the p_{μ^+} determination is located at different microstrips for the different settings. The six p_{μ^+} results in each of the two plots in Fig. 14 show no significant dependence on the spectrometer setting, as expected.

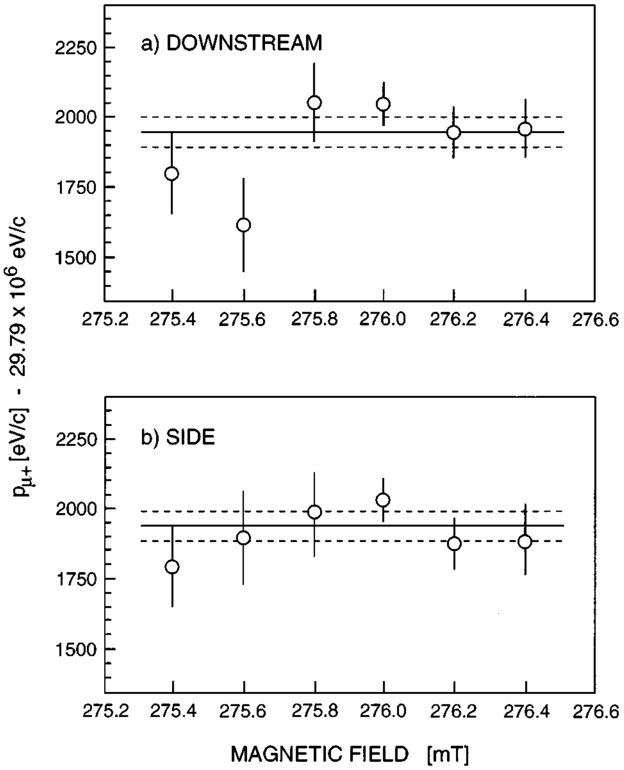

FIG. 14. Uncorrected experimental results for the muon momentum p_{μ^+}, as a function of the spectrometer field, (a) for muons from the downstream surface of the production target, (b) for muons from the side surface.

For the standard deviation w of the Gaussian distribution with which the theoretical muon-momentum spectra were folded [parameter (4) of Sec. V B above], the following weighted means were obtained:

$$w(\text{downstream})=(5.085\pm 0.040)\ \text{keV}/c, \quad (16)$$

with $\chi^2=29.6$ (21 DF),

$$w(\text{side})=(4.897\pm 0.040)\ \text{keV}/c, \quad (17)$$

with $\chi^2=13.4$ (21 DF).

D. Target surface correction

The difference between the experimental results of Eqs. (14) and (15) is

$$Dp=p_{\mu^+}(\text{downstream})-p_{\mu^+}(\text{side})$$
$$=(0.002\pm 0.077)\ \text{keV}/c. \quad (18)$$

This differs from the theoretical prediction for smooth target surfaces given by Eq. (9) [Sec. IV A], but is consistent with the more plausible prediction for grainy surfaces, Eq. (12). Since the correction for the downstream surface is smaller than that for the side surface, and is almost independent of the assumed surface structure [cf. Eqs. (7) and (10)], we used for the final determination of p_{μ^+} the 22 downstream-surface spectra only. To the value given by Eq. (14) we added a surface correction of

$$\delta p_{\mu^+} = (+51 \pm 51) \ \text{eV}/c. \tag{19}$$

The most probable value given by Eq. (19) is the average of Eqs. (7) and (10), whereas the uncertainty in Eq. (19) was chosen to be equal to the most probable value, and thus larger than the uncertainties in Eqs. (7) and (10). By this conservative estimate, we took into account that the Monte-Carlo calculation of the surface shift (Sec. IV A) contains fairly crude approximations [4, 5].

E. Kinetic energy of trapped pions

The extension of the cutoff in the experimental spectra (e.g., in microstrips 185–195 of Fig. 12) was significantly larger than that expected for pions decaying exactly at rest. We attribute that extension mainly to a Doppler broadening of the muon momentum distribution caused by the motion of the trapped pions. In order to calculate the mean kinetic energy of the pions just before their decay from the standard deviation w obtained by the fits [cf. Eqs. (16) and (17)], a number of additional broadening effects must be considered [9].

(1) In the Monte Carlo spectra the microstrip number is defined by the point where the muon hits the detector, whereas in the experimental spectra the microstrip number is defined by the highest charge (Sec. III A). Because of the effects discussed in Sec. IV E above, the highest charge can occur in the wrong strip if the muon hits the detector close to a strip boundary [9]. The corresponding spatial standard deviation was found to be 16±1 μm, which corresponds to a momentum standard deviation of

$$\sigma_M = (0.66 \pm 0.04) \ \text{keV}/c. \tag{20}$$

Other broadening effects, considered below, were found to be negligible compared to the standard deviations w given by Eqs. (16) and (17).

(2) The reduced pion stop density in the outermost few nanometers of the graphite target [cf. Fig. 9 and Eqs. (5) and (6)]. This broadening is of the same order as the corrections given by Eqs. (10) and (11).

(3) The momentum broadening caused by decay positrons [cf. Fig. 5(b)], which in rare cases can distort the microstrip charge distribution [18].

(4) The multiple scattering and energy loss straggling of the muons in the residual gas in the vacuum chambers of the beam line and the spectrometer (pressure $\approx 6 \times 10^{-6}$ mbar).

(5) The rare radiative pion decay, $\pi^+ \to \mu^+ \nu_\mu \gamma$.

The standard deviation $\sigma_{p_{\mu^+}}$ of the muon-momentum broadening due to the motion of the decaying pion is thus obtained from Eqs. (16), (17), and (20) by quadratical subtraction, $\sigma_{p_{\mu^+}} = [w^2 - \sigma_M^2]^{1/2}$:

$$\sigma_{p_{\mu^+}}(\text{downstream}) = (5.042 \pm 0.040) \ \text{keV}/c, \tag{21}$$

$$\sigma_{p_{\mu^+}}(\text{side}) = (4.852 \pm 0.040) \ \text{keV}/c. \tag{22}$$

For all isotropic distributions of nonrelativistic pions, there is a general relation between the standard deviation $\sigma_{p_{\mu^+}}$ and the mean kinetic energy $\overline{T_\pi}$ of the pions [4]:

$$\sigma_{p_{\mu^+}} = E_{\mu^+}[2\overline{T_\pi}/(3m_\pi)]^{1/2}. \tag{23}$$

Here, $E_{\mu^+} = 109.78$ MeV is the total muon energy in π^+ decay at rest, and m_π is the π^+ mass. Equations (21)–(23) lead to the mean kinetic pion energies

$$\overline{T_\pi}(\text{downstream}) = (0.442 \pm 0.007) \ \text{eV}, \tag{24}$$

$$\overline{T_\pi}(\text{side}) = (0.409 \pm 0.007) \ \text{eV}. \tag{25}$$

The uncertainties in Eqs. (24) and (25) are statistical only. These mean pion energies are significantly higher than the mean energy of 0.128–0.164 eV valid for a Maxwell-Boltzmann distribution of free pions or ($\pi^+ e^-$) atoms at the graphite target temperatures of 990–1270 K. On the other hand, Eqs. (24) and (25), and also the assumed Gaussian muon-momentum distribution [cf. free parameter (4) of Sec. V B above], agree with the hypothesis that the pions are trapped in the potential well of a spherical harmonic oscillator as derived by Shirasu *et al.* [14], from their measurements of the solubility of low-pressure hydrogen and deuterium in isotropic graphite.

The difference between Eqs. (24) and (25) (3.3 standard deviations) may be due to the fact that the radiation damage to the target at the downstream surface, which is hit directly by the proton beam (cf. Fig. 1), is more severe than that at the side surface, so that the distribution of the pions to various possible trapping sites is different in the two cases. If one neglects these differences and combines Eqs. (24) and (25), one obtains the final estimate

$$\overline{T_\pi} = (0.425 \pm 0.016) \ \text{eV} \tag{26}$$

for the mean kinetic energy of the pions immediately before their decay. The uncertainty in Eq. (26) was chosen such that the central values of Eqs. (24) and (25) are included in the error bar.

If the pions are assumed to be trapped in the potential of a spherical harmonic oscillator,

$$V(r) = V_0 + \tfrac{1}{2} k_s r^2, \tag{27}$$

where r is the distance from the center of the potential, then the mean pion energy of Eq. (26) corresponds [4] to a spring constant of

$$k_s = (1.144 \pm 0.088) \times 10^{17} \text{eV}/\text{cm}^2. \tag{28}$$

The oscillation frequency of protons trapped in the potential defined by Eqs. (27) and (28) is

$$\nu_H = (1757 \pm 67) \ \text{cm}^{-1}. \tag{29}$$

This is consistent with the result $\nu_H \approx 1600 \ \text{cm}^{-1}$, obtained by Shirasu *et al.* [14] from their hydrogen and deuterium solubility measurements.

TABLE I. Contributions to the uncertainty of the muon momentum p_{μ^+}.

Source of uncertainty	Uncertainty (eV/*c*)
(1) ''Statistical'' uncertainties:	
1.1. MINUIT error (counting statistics and microstrip efficiencies)	± 47
1.2. Scatter of position measurements	± 26
1.3. Scatter of magnetic field maps	± 35
1.4. Monte Carlo statistics	± 9
Quadratic sum (1)	± 65
(2) Systematic uncertainties:	
2.1. Position measurement device	± 15
2.2. Magnetic-field measurement device	± 67
2.3. Muon energy loss in graphite target	± 22
2.4. Graphite-target surface correction	± 51
2.5. Charge drift in microstrip detector	± 7
2.6. Atomic potential at μ^+ creation	± 0.4
2.7. Muon energy loss in residual gas	± 0.6
Quadratic sum (2)	± 89
Quadratic sum (1,2)	± 110

F. Momentum of muons from pion decay at rest

The p_{μ^+} value obtained from the fits to the spectra of muons from the downstream surface of the production target is given by Eq. (14) above. To that value, several corrections had to be added.

(1) The target surface correction of Eq. (19), $(+51\pm 51)$ eV/c.

(2) A ''Hall effect'' correction taking into account the deflection of the charge carriers in the microstrip detector by the magnetic field of the spectrometer [9], (-49 ± 7) eV/c.

(3) A correction due to the trap potential in the graphite target, which the muons have to surmount. From the enthalpy of solution for hydrogen in graphite, measured by Shirasu *et al.* [14], it follows that the protons of hydrogen trapped in graphite have a binding energy of 16.08 eV. We assume that the trap potential for pions is the same as that for protons (cf. Sec. V E above). This leads to a pion binding energy of (15.6 ± 0.1) eV [9], which the decay muons have to surmount in leaving the site of their creation. The corresponding p_{μ^+} correction is $(+57.5\pm 0.4)$ eV/c.

(4) The correction for the energy loss of the muons on their way through the residual gas in the vacuum chambers of the beam line and the spectrometer [pressure $(6\pm 4)\times 10^{-6}$ mbar], amounting to $(+0.9\pm 0.6)$ eV/c.

Our final result for the momentum of muons from the decay $\pi^+\rightarrow\mu^+\nu_\mu$ at rest is thus

$$p_{\mu^+}=(29.791\,998\pm 0.000\,065_{\text{stat}}\pm 0.000\,089_{\text{syst}})\ \text{MeV}/c. \tag{30}$$

The contributions to the statistical and systematic uncertainties in Eq. (30) are listed in Table I. If these two uncertainties are added in quadrature, one obtains

$$p_{\mu^+}=(29.792\,00\pm 0.000\,11)\ \text{MeV}/c. \tag{31}$$

The relative uncertainty of p_{μ^+} is thus ± 3.7 ppm.

The result of Eq. (31) is consistent with the value of p_{μ^+} obtained by use of a π^+ beam [1], but is more precise by a factor of 4.8 . The most probable value of the new result is lower by 0.07 keV/c than that given in our recent letter [3] on the present experiment. The difference is mostly due to a correction in the analysis of the distance measurements (cf. Sec. II D above) of Ref. [3], and also to the inclusion of a few additional muon spectra in the present analysis. The result given by Eq. (31) is intended to replace that of Ref. [3].

VI. CONCLUSIONS

A. Upper limit of the muon-neutrino mass

We use the p_{μ^+} value of Eq. (31), together with measurements of the μ^+ and π^- masses and the CPT theorem $(m_{\pi^+}=m_{\pi^-})$, to derive a new value of the squared muon-neutrino mass. The μ^+-mass is taken from Ref. [19]:

$$m_{\mu^+}=(105.658\,389\pm 0.000\,034)\ \text{MeV}. \tag{32}$$

For the π^- mass, we use each of the two possible values derived in the recent reanalysis [20] of the pionic x-ray spectrum of Jeckelmann *et al.* [21]: i.e.,

$$m_{\pi^-}(A)=(139.567\,82\pm 0.000\,37)\ \text{MeV}, \tag{33}$$

or

$$m_{\pi^-}(B)=(139.569\,95\pm 0.000\,35)\ \text{MeV}. \tag{34}$$

The value $m_{\pi^-}(A)$ of Eq. (33) is obtained if, in the calculation of the electron-screening correction, the strongest component of the pionic magnesium $(4f\rightarrow 3d)$ x-ray line of Ref. [21] is assumed to correspond to the presence of one K electron, whereas the value $m_{\pi^-}(B)$ of Eq. (34) results if the strongest component is assumed to correspond to the presence of two K electrons.

For the smaller of the two π^- mass values, i.e., for Eqs. (31)–(33), four-momentum conservation in the decay $\pi^+\rightarrow\mu^+\nu_\mu$ [cf. Eq. (2) above] leads to the squared muon-neutrino mass

$$m_{\nu_\mu}{}^2(A)=(-0.143\pm 0.024)\ \text{MeV}^2, \tag{35}$$

whereas the larger of the two π^--mass values [Eqs. (31),(32), and (34)] leads to

$$m_{\nu_\mu}{}^2(B)=(-0.016\pm 0.023)\ \text{MeV}^2. \tag{36}$$

The first of the two $m_{\nu_\mu}{}^2$ values [Eq. (35)], negative by six standard deviations, can be considered as unphysical and thus excludes the smaller of the two π^- mass values [Eq. (33)]. The second $m_{\nu_\mu}{}^2$ value [Eq. (36)], on the other hand, is compatible with zero, and hence implies that the larger of the two π^- mass values [Eq. (34)] is consistent with our new p_{μ^+} result. Thus we conclude that the squared muon-neutrino mass is as given by Eq. (36) above. According to the ''Bayesian approach'' described by the Particle Data Group (page 1280 of Ref. [19]; probability density set to zero for $m_{\nu_\mu}{}^2<0$), Eq. (36) corresponds to the new upper limit

$$m_{\nu_\mu} < 0.17 \text{ MeV (C.L.} = 0.9). \tag{37}$$

The uncertainty of the squared neutrino mass in Eq. (36), and thus also the upper limit of m_{ν_μ} [Eq. (37)], is dominated by the m_{π^-} uncertainty [cf. Eqs. (3) and (4)].

B. Mass of π^+ "with cosmology"

The following π^+ mass is derived from the p_{μ^+} value of Eq. (31), the μ^+ mass of Eq. (32) and the assumption $m_{\nu_\mu} = 0$:

$$m_{\pi^+} = (139.570\,22 \pm 0.000\,14) \text{ MeV}. \tag{38}$$

For muon-neutrino masses below the cosmological upper limit, $m_{\nu_\mu} < 65$ eV [22], the resulting π^+-mass is equal to that of Eq. (38).

C. Mass of $\pi^\pm$ "without cosmology"

If the cosmological m_{ν_μ} limit is not used, then the new p_{μ^+} result of Eq. (31) and the m_{μ^+} value [19] lead either to the m_{π^+} result given by Eq. (38) above (for $m_{\nu_\mu} = 0$) or to larger m_{π^+} values (for $m_{\nu_\mu} \neq 0$). This information, the m_{π^-} results [19], and the CPT theorem ($m_{\pi^+} = m_{\pi^-}$) together lead to a value of $m_{\pi^\pm}$ which is more precise than the m_{π^-} results alone. This can be demonstrated by considering, e.g., a tentative $m_{\pi^\pm}$ value of 139.569 60 MeV. This value is at the lower end of the error bar of the m_{π^-} result given by Eq. (34), but is lower than the new m_{π^+} result obtained from p_{μ^+} by 4.4 standard deviations [for $m_{\nu_\mu} = 0$; cf. Eq. (38)] or more (for $m_{\nu_\mu} \neq 0$).

The relevant two-dimensional probability distributions are illustrated in Fig. 15. The two vertical bands in Fig. 15(a) correspond to the m_{π^-} results of Ref. [20]; cf. Eqs. (33) and (34) above. The tilted band in Fig. 15(a) indicates the $m_{\nu_\mu}^2$ value derived from p_{μ^+} and m_{μ^+} as a function of the assumed value of m_{π^+}. The combined probability density differs significantly from zero in the regions where the bands intersect. The lower of the two intersections in Fig. 15(a) is located at negative $m_{\nu_\mu}^2$ and thus is excluded. The upper intersection is shown in greater detail in Fig. 15(b). Our final estimate of the charged-pion mass *without cosmology* is derived from Fig. 15(b) by the following procedure [23]:

(1) The probability density function $f(m_{\pi^\pm}, m_{\nu_\mu}^2)$ is set to zero for negative values of $m_{\nu_\mu}^2$. (2) The remaining density function is projected onto the $m_{\pi^\pm}$ axis of Fig. 15(b); i.e., the probability density function $h(m_{\pi^\pm}) \equiv \int_0^{+\infty} f(m_{\pi^\pm}, m_{\nu_\mu}^2) d(m_{\nu_\mu}^2)$ is calculated.

(3) The mean and variance of the resulting slightly asymmetric distribution function $h(m_{\pi^\pm})$ lead to the result

$$m_{\pi^\pm} = (139.570\,37 \pm 0.000\,21) \text{ MeV}, \tag{39}$$

this agrees with the result *with cosmology* of Eq. (38).

D. Comparison with previous $\pi^\pm$-mass results

In comparison with the recent reanalysis by Jeckelmann *et al.* [20], the π^+ mass of Eq. (38) agrees with the $m_\pi(B)$ value of Eq. (34), but excludes the $m_\pi(A)$ value of Eq. (33) by six standard deviations. Considering the older $m_{\pi^\pm}$ results compiled in the meson full listings of the 1994 Particle Data Group (p. 1446 of Ref. [19]), the pion mass of Eq. (38) agrees with the values DAUM 91 and ABELA 84, but is larger by several standard deviations than the values JECKELMANN 86 and LU 80; cf. Fig. 16. The discrepancy be-

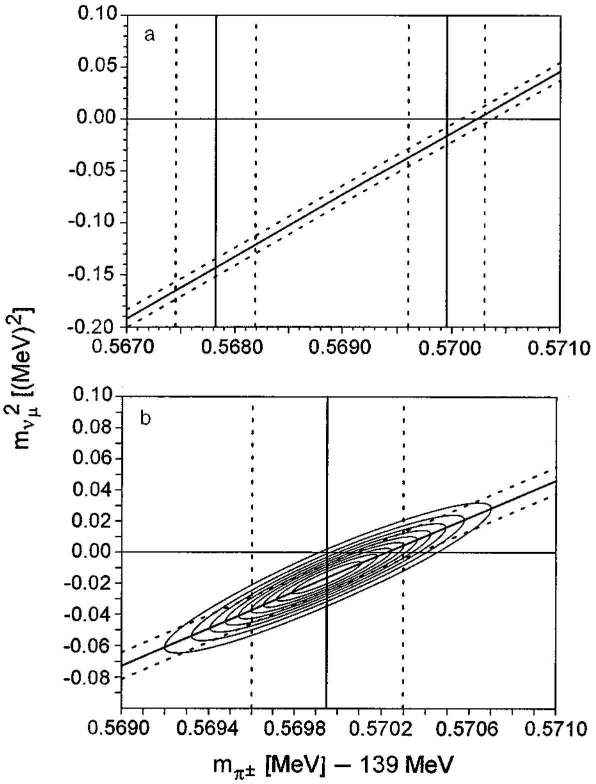

FIG. 15. Allowed regions of the $(m_{\pi^\pm}, m_{\nu_\mu}^2)$-plane. Band widths correspond to ±1 standard deviation. The concentric ellipses in (b) are lines of constant probability density, at $0.1f_0$, $0.2f_0$, ... , $0.9f_0$ (where f_0 is the central density).

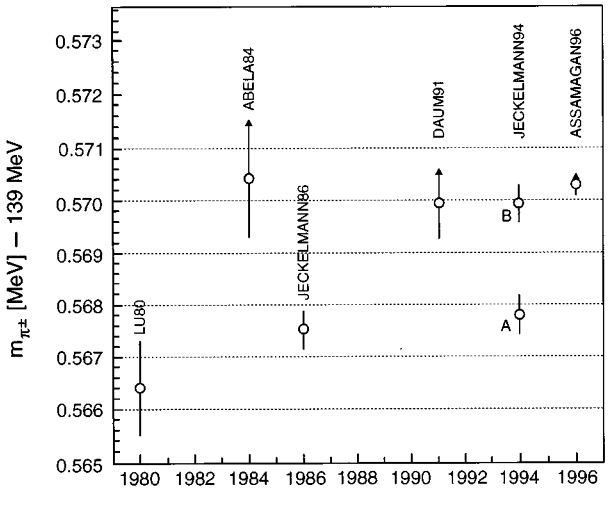

FIG. 16. Recent $\pi^\pm$-mass measurements; cf. p. 1446 of Ref. [19]. The values ABELA84, DAUM91, and ASSAMAGAN96 [Eq. (38) of present paper] are based on p_{μ^+} measurements; values above the vertical arrows are possible if $m_{\nu_\mu} \neq 0$.

tween Eq. (38) and JECKELMANN 86 can be explained by the fact that the latter value was based on ‘‘solution *A*’’ (strongest component of the x-ray line attributed to presence of one *K* electron), which according to the reanalysis [20] is no longer preferred over solution *B*.

E. Kinetic energy of π^+ mesons stopped in graphite

The mean kinetic energy of π^+ mesons stopped in isotropic graphite at temperatures of 990–1270 K immediately before their decay is determined to be (0.425 ± 0.016) eV [cf. Eq. (26) above]; if the pions are assumed to be trapped in the potential well of a spherical harmonic oscillator, $V(r)=V_0+(1/2)k_s r^2$, then the spring constant is derived to be $k_s=(1.144\pm0.088).10^{17}\mathrm{eV/cm}^2$. This trap potential agrees with that derived from measurements of the solubility of hydrogen and deuterium in isotropic graphite [14].

ACKNOWLEDGMENTS

We wish to thank Dr. P. F. A. Goudsmit, Professor P.F. Meier and Dr. U. Rohrer for discussions, H. Oesch for collaboration in the distance measurements, E. Barthazy, B. Henrich, and J. Löffler for participation in the data taking and analysis, P. Dick for work on electronics problems, D. C. George for help with the magnetic spectrometer, S. Streuli for assistance with the microstrip detector, and many other PSI staff members for their support.

---

[1] M. Daum *et al.*, Phys. Lett. B **265**, 425 (1991).
[2] M. Daum *et al.*, Phys. Rev. D **20**, 2692 (1979).
[3] K. Assamagan *et al.*, Phys. Lett. B **335**, 231 (1994).
[4] R. Frosch, J. Löffler, and C. Wigger, Paul Scherrer Institute Report No. TM-11-92-01, 1992 (unpublished).
[5] R. Frosch and C. Wigger, Paul Scherrer Institute Report No. TM-11-94-01, 1994 (unpublished).
[6] K.L. Brown *et al.*, CERN Report No. 73-16, 1973 (unpublished).
[7] Th. Spirig, Diplomarbeit, University of Zürich, 1992.
[8] R. Abela *et al.*, Phys. Lett. **146B**, 431 (1984).
[9] C. Wigger, Ph.D. thesis, University of Zürich, 1995.
[10] J.F. Crawford *et al.*, Phys. Rev. C **22**, 1184 (1980).
[11] J.F. Crawford *et al.*, Helv. Phys. Acta **53**, 497 (1980).
[12] J.F. Ziegler *et al.*, *The Stopping and Range of Ions in Solids* (Pergamon Press, New York, 1985).
[13] E. Hoinkis, J. Nucl. Mater. **182**, 93 (1991).
[14] Y. Shirasu *et al.*, J. Nucl. Mater. **179-181**, 223 (1991).
[15] H. Bichsel, Rev. Mod. Phys. **60**, 663 (1988).
[16] R. Frosch and D. Herter, Paul Scherrer Institute Report No. TM-11-90-01, 1990 (unpublished).
[17] F. James and M. Roos, CERN Program Library, D506, MINUIT, Function Minimization and Error Analysis, 1989.
[18] Ch. Brönnimann, Diplomarbeit, University of Zürich, 1992.
[19] Particle Data Group, Phys. Rev. D **50**, 1173 (1994).
[20] B. Jeckelmann, P.F.A. Goudsmit, and H.J. Leisi, Phys. Lett. B **335**, 326 (1994).
[21] B. Jeckelmann *et al.*, Nucl. Phys. **A457**, 709 (1986).
[22] H. Harari and Y. Nir, Nucl. Phys. **B292**, 251 (1987).
[23] R. Frosch, Paul Scherrer Institute Report No. TM-11-94-03, 1994 (unpublished).